

Three-dimensional lattice Boltzmann model for immiscible two-phase flow simulationsHaihu Liu^{*} and Albert J. Valocchi[†]*Department of Civil & Environmental Engineering, University of Illinois at Urbana-Champaign, Urbana, Illinois 61801, USA*Qinjun Kang[‡]*Earth and Environmental Sciences Division, Los Alamos National Laboratory, Los Alamos, New Mexico 87545, USA*

(Received 16 January 2012; published 20 April 2012)

We present an improved three-dimensional 19-velocity lattice Boltzmann model for immiscible binary fluids with variable viscosity and density ratios. This model uses a perturbation step to generate the interfacial tension and a recoloring step to promote phase segregation and maintain surfaces. A generalized perturbation operator is derived using the concept of a continuum surface force together with the constraints of mass and momentum conservation. A theoretical expression for the interfacial tension is determined directly without any additional analysis and assumptions. The recoloring algorithm proposed by Latva-Kokko and Rothman is applied for phase segregation, which minimizes the spurious velocities and removes lattice pinning. This model is first validated against the Laplace law for a stationary bubble. It is found that the interfacial tension is predicted well for density ratios up to 1000. The model is then used to simulate droplet deformation and breakup in simple shear flow. We compute droplet deformation at small capillary numbers in the Stokes regime and find excellent agreement with the theoretical Taylor relation for the segregation parameter $\beta = 0.7$. In the limit of creeping flow, droplet breakup occurs at a critical capillary number $0.35 < Ca_c < 0.4$ for the viscosity ratio of unity, consistent with previous numerical simulations and experiments. Droplet breakup can also be promoted by increasing the Reynolds number. Finally, we numerically investigate a single bubble rising under buoyancy force in viscous fluids for a wide range of Eötvös and Morton numbers. Numerical results are compared with theoretical predictions and experimental results, and satisfactory agreement is shown.

DOI: [10.1103/PhysRevE.85.046309](https://doi.org/10.1103/PhysRevE.85.046309)

PACS number(s): 47.55.Ca, 47.11.-j

I. INTRODUCTION

Numerical modeling and simulation of immiscible multiphase flows have received wide attention over the last 20 years, as such flows are involved in many aspects of basic fluid mechanics as well as in engineering and environmental problems. Traditionally, multiphase flows are simulated by solving the macroscopic Navier-Stokes equations (NSEs) that govern the physics of fluids together with a proper technique to track or capture the interface between different phases. Among the approaches, the front-tracking method [1–3], volume-of-fluid (VOF) method [4–7], and level set method [8–10] are commonly used. The front-tracking method is not suitable for simulating interface breaking and coalescing, because the interface must be manually ruptured based upon some *ad hoc* criteria [2]. VOF and level set methods can naturally deal with interface breaking and coalescing, and both solve a pure advection equation for the interface in the Eulerian frame. However, interface reconstruction is required in the VOF method to determine the interfacial tension force and calculate the flux across the interface. This process can be time consuming and not always physically consistent [11]. Also, most of the VOF interface reconstruction schemes are only first-order accurate. The level set method uses a signed distance function to represent the interface. It requires a reinitialization procedure to keep the distance property when large topological changes occur around the interface.

This may violate the mass conservation for each phase or component. In addition, VOF and level set methods will suffer from numerical instability at the interface region when the interfacial tension becomes a dominant factor in complex geometries [12]. For example, it is challenging to apply VOF or level set methods to simulate capillary displacement in porous media. Microscopically, the phase segregation and the interfacial dynamics between different phases are due to interparticle forces or interactions [13,14]. Thus, mesoscopic level models are expected to describe accurately the complex dynamic behavior of multiphase flows.

In recent years, the lattice Boltzmann method (LBM) has emerged as an attractive numerical tool for simulating multiphase flow problems [15,16]. Unlike traditional numerical methods, which are based on the solution of macroscopic variables such as velocity and density, the LBM is a pseudomolecular method that tracks evolution of the particle distribution function of an assembly of molecules and is built upon microscopic models and mesoscopic kinetic equations [17]. The macroscopic variables can be obtained from the moment integrations of the particle distribution function. As such, the LBM has several advantages over the traditional numerical methods such as the ability to be programmed on parallel computers and the ease in dealing with complex boundaries [18]. Besides, its mesoscopic nature provides many of the advantages of molecular dynamics, making the LB method especially effective for simulation of complex interfacial dynamics [19–23].

Several lattice Boltzmann models have been proposed for simulating multiphase flows. The color-fluid model was proposed by Gunstensen *et al.* [24] based on the

^{*}haihuliu@illinois.edu[†]valocchi@illinois.edu; <https://netfiles.uiuc.edu/valocchi/www/>[‡]qkang@lanl.gov

Rothman-Keller lattice gas model [25]. Two kinds of colored particles (red and blue) are introduced to distinguish different fluids. The local color flux and color gradient are calculated and the work done by the color gradient against the color flux is maximized to force the colored particles to move toward fluids with the same color (this is known as the recoloring step). A perturbation step is applied to realize the interfacial tension effect. Later, Grunau *et al.* [26] modified this model to allow for variations of density and viscosity. However, the density ratio is restricted to around 1 for the color-fluid model; in addition, the procedure to separate different phases requires time-consuming calculations to find local maxima, and the perturbation step can cause an anisotropic interfacial tension that induces high spurious velocities near an interface [18]. The pseudopotential model developed by Shan and Chen [27] introduces the nearest-neighbor interaction between fluid particles to describe the intermolecular potential, and the phase separation occurs with a properly chosen potential function. Although significant advances have recently been made [28–30], further improvements are necessary for the pseudopotential model to minimize spurious velocities at interfaces and control numerical instability for flows with low capillary number and high viscosity ratio [22]. The free-energy model presented by Swift *et al.* [31] introduces phase effects directly into the collision process by considering a generalized equilibrium distribution function that includes a nonideal pressure tensor term. These terms are defined to cohere with the free-energy functional in diffuse-interface theory. In contrast to the previous LB multiphase models, this model is shown to be thermodynamically consistent. Although the free-energy model satisfies the local conservation of mass and momentum, it suffers from the lack of Galilean invariance except for a binary fluid with equal densities. In addition, small droplets are prone to dissolve since the multiphase system is always evolving toward the direction of minimal free energy [21,32]. The mean-field model proposed by He *et al.* [13] introduces the interfacial dynamics by incorporating molecular interaction forces, which are approximated by the mean-field theory. This model uses an index function to track interfaces, and its numerical stability is enhanced by reducing the discretization errors in calculation of molecular interactions. However, the density ratio is restricted to a maximum of about 15 due to the “stiffness” of the collision operator [33]. In addition, the mobility in the interface-capturing equation is related to the density and cannot be flexibly chosen [34]. Lately, several LB multiphase models have emerged to tackle large-density-ratio problems [34–37]. Most of them demand high computing cost and/or complex numerical schemes [35,37]. Like the free-energy model, these models cannot ensure the mass conservation for each fluid due to numerical dissipation, which becomes much worse for small droplets or bubbles in the three-dimensional domain; see, e.g., Ref. [38].

Based on the original color-fluid model of Gunstensen *et al.*, some improvements have been made to model the interfacial tension and reduce the spurious velocities at the interface. Lishchuk *et al.* [39] used the concept of a continuum surface force (CSF) [40] to model the interfacial tension. In their algorithm, the perturbation step in the original Gunstensen *et al.* model was replaced by a direct forcing term in the mixed region. This forcing term is used to

recover the required pressure gradient across the interface, and is calculated explicitly from the interfacial normal and the macroscopic curvature of the interface. It has been reported that this algorithm can greatly reduce the spurious currents and improve the isotropy of the interface. However, this algorithm needs additional calculation for the derivatives of the interfacial normal to obtain the curvature, which leads to difficulties in simulating contact angles because more information is required at walls compared to the original Gunstensen *et al.* model. Also, only equal density is considered for both fluids. Latva-Kokko and Rothman [41] identified the problem of lattice pinning exhibited by the recoloring step in the original Gunstensen *et al.* model and proposed a new algorithm for the recoloring step, which allows the red and the blue fluids to moderately mix at the tangent of the interface and keeps the color distribution symmetric with respect to the color gradient. Wu *et al.* [42] found that the recoloring algorithm proposed by Latva-Kokko and Rothman can resolve the adverse side-effect problem, which induces anisotropy and high spurious velocities at the interface. Recently, Reis and Phillips [43] developed a two-dimensional nine-velocity LB model for immiscible binary fluids with variable viscosities and density ratios. A new perturbation operator was proposed to recover the correct NSEs for two-phase flows. A theoretical expression for interfacial tension was derived through its mechanical definition and some approximations. However, this model is limited to two dimensions; in addition, it preserves the recoloring algorithm in the original Gunstensen *et al.* model and uses second-order anisotropic discretization for the color gradient, which greatly restricts the accuracy and stability of model. By extending the model of Grunau *et al.* [26], Tölke *et al.* [44] constructed a three-dimensional 19-velocity LB model for immiscible binary fluids. It can be shown that this model cannot produce the correct form for the interfacial force. In order to accurately reproduce multiphase flows in the real world, a three-dimensional LB model is urgently required, which has high accuracy, low spurious velocities, and the capability to simulate fluids with variable viscosities and density ratios.

In this work, we present an improved LB color-fluid model for simulating three-dimensional immiscible binary fluids with variable viscosity and density ratios. A generalized perturbation operator is derived using the concept of a continuum surface force together with the constraints of mass and momentum conservation. In order to generate isotropic interfacial tension and reduce the spurious velocities, we use fourth-order isotropic discretization for the gradient of the phase field, as in Refs. [45–47]. A theoretical expression for the interfacial tension parameter is obtained directly without any additional analysis or assumptions. In addition, a recoloring algorithm proposed by Latva-Kokko and Rothman [41] is applied for phase segregation, which minimizes the spurious velocities even further, and at the same time overcomes lattice pinning. Finally, extensive numerical simulations are conducted to validate the capability and accuracy of this model. These include simulation of a static bubble for interfacial tension, droplet deformation and breakup in simple shear flow, and buoyancy-driven motion of a single bubble. The numerical results are compared with theoretical and numerical predictions as well as experimental data. We should mention

that, in the present model, different contact angles can be obtained easily through adjustment of the value of the phase field at the solid surface [48].

II. THEORY AND MATHEMATICAL MODEL

In this model, red and blue particle distribution functions f_i^R and f_i^B are introduced to represent two different fluids. The total particle distribution function is defined as $f_i = f_i^R + f_i^B$. Each of the colored phases undergoes the collision and streaming operators

$$f_i^k(\mathbf{x} + \mathbf{e}_i \delta_t, t + \delta_t) = f_i^k(\mathbf{x}, t) + \Omega_i^k(\mathbf{x}, t), \quad (1)$$

where the superscript $k = R$ or B denotes the color ("red" or "blue"), $f_i(\mathbf{x}, t)$ is the particle distribution function in the i th velocity direction at position \mathbf{x} and time t , \mathbf{e}_i is the lattice velocity in the i th direction, δ_t is the time step, and Ω_i^k is the collision operator. The collision operator is the result of the combination of three suboperators [44]:

$$\Omega_i^k = (\Omega_i^k)^{(3)} [(\Omega_i^k)^{(1)} + (\Omega_i^k)^{(2)}], \quad (2)$$

where $(\Omega_i^k)^{(1)}$ is the Bhatnagar-Gross-Krook (BGK) collision operator, $(\Omega_i^k)^{(2)}$ is a two-phase collision operator (perturbation step) which contributes to the mixed interfacial region and

generates an interfacial tension, and $(\Omega_i^k)^{(3)}$ represents the "recoloring," which mimics the phase segregation and keeps the interface sharp.

In the BGK collision operator, the particle distribution functions are relaxed toward a local equilibrium with a single relaxation time:

$$(\Omega_i^k)^{(1)} = -\frac{1}{\tau_k} (f_i^k - f_i^{k,\text{eq}}), \quad (3)$$

where τ_k is the dimensionless relaxation time of fluid k , and $f_i^{k,\text{eq}}$ is the equilibrium distribution function of f_i^k . Conservation of mass for each phase and total momentum conservation require

$$\rho_k = \sum_i f_i^k = \sum_i f_i^{k,\text{eq}}, \quad (4)$$

$$\rho \mathbf{u} = \sum_i \sum_k f_i^k \mathbf{e}_i = \sum_i \sum_k f_i^{k,\text{eq}} \mathbf{e}_i, \quad (5)$$

where ρ_k is the density of fluid k , $\rho = \rho_R + \rho_B$ is the total density, and \mathbf{u} is the local fluid velocity.

For the three-dimensional 19-velocity (D3Q19) model, the lattice velocity \mathbf{e}_i and the weight coefficients w_i are given as follows:

$$\mathbf{e}_i = \begin{cases} (0,0,0), & i = 0, \\ (\pm 1, 0, 0)c, (0, \pm 1, 0)c, (0, 0, \pm 1)c, & i = 1, 2, \dots, 6, \\ (\pm 1, \pm 1, 0)c, (\pm 1, 0, \pm 1)c, (0, \pm 1, \pm 1)c, & i = 7, 8, \dots, 18, \end{cases} \quad (6)$$

$$w_i = \begin{cases} 1/3, & i = 0, \\ 1/18, & i = 1, 2, \dots, 6, \\ 1/36, & i = 7, 8, \dots, 18, \end{cases} \quad (7)$$

where $c = \delta_x / \delta_t$ is the lattice speed with δ_x being the lattice length. The equilibrium distribution functions are chosen to respect the conservation constraints of Eqs. (4) and (5), and are defined by

$$f_i^{k,\text{eq}} = \rho_k \left(\phi_i^k + w_i \left[\frac{3}{c^2} \mathbf{e}_i \cdot \mathbf{u} + \frac{9}{2c^4} (\mathbf{e}_i \cdot \mathbf{u})^2 - \frac{3}{2c^2} \mathbf{u}^2 \right] \right), \quad (8)$$

where

$$\phi_i^k = \begin{cases} \alpha_k, & i = 0, \\ (1 - \alpha_k)/12, & i = 1, 2, \dots, 6, \\ (1 - \alpha_k)/24, & i = 7, 8, \dots, 18. \end{cases} \quad (9)$$

In the above equation, α_k is a free parameter, which determines the speed of sound c_s^k , thus controlling the hydrodynamic pressure in the fluids. The pressure of fluid k is given as

$$p_k = \rho_k (c_s^k)^2 = \frac{\rho_k (1 - \alpha_k)}{2}. \quad (10)$$

For a flat two-phase interface in a quiescent system (e.g., the layered flow of two immiscible fluids with different densities between two parallel plates), the pressure across the interface should be continuous, i.e., $p_R = \rho_R \frac{1 - \alpha_R}{2} = p_B = \rho_B \frac{1 - \alpha_B}{2}$, which indicates that the density ratio needs to be taken as [43,44]

$$\lambda = \frac{\rho_R}{\rho_B} = \frac{1 - \alpha_B}{1 - \alpha_R}. \quad (11)$$

Note that α_k should satisfy the condition $0 < \alpha_k < 1$ in order to avoid negative pressures and equilibrium distribution functions.

The relaxation time τ_k is chosen so that Eq. (1) recovers the macroscopic equations for single-phase flows in each single-phase region. It is a function of the kinematic viscosity of fluid and given by (see the Appendix for the derivation)

$$v_k = \frac{c^2}{3} \left(\tau_k - \frac{1}{2} \right) \delta_t. \quad (12)$$

To account for unequal viscosities of both fluids, a linear interpolation is used to determine the relaxation time τ at

the interface [44], i.e.,

$$\tau = \frac{1 + \rho^N}{2} \tau_R + \frac{1 - \rho^N}{2} \tau_B, \quad (13)$$

where the phase field ρ^N is defined as

$$\rho^N(\mathbf{x}, t) = \frac{\rho_R(\mathbf{x}, t) - \rho_B(\mathbf{x}, t)}{\rho_R(\mathbf{x}, t) + \rho_B(\mathbf{x}, t)}, \quad -1 \leq \rho^N \leq 1. \quad (14)$$

The values of the phase field $\rho^N = 1, -1$, and 0 correspond to a purely red fluid, a purely blue fluid, and the interface, respectively.

In the color-fluid model, the perturbation operator is used to model the interface tension. As can be shown below, direct extension of the model of Grunau *et al.* [26], which models immiscible fluid flows with different density ratios and viscosities on a two-dimensional hexagonal lattice, to the D3Q19 lattice fails to obtain the correct interfacial force. In this study, we will use the concept of a continuum surface force to construct the perturbation operator, which can reduce the spurious currents and improve the isotropy of the interface. More importantly, we build a bridge between the mesoscopic interparticle interactions and the macroscopic description of interfacial force. In addition, an expression for the interfacial tension parameter is directly obtained without any additional analysis and approximations. It is worth mentioning that this method is different from the algorithm proposed by Lishchuk *et al.* [39] which also uses the CSF to model the interfacial force. In their algorithm, the macroscopic interfacial force is calculated explicitly through the interfacial normal and macroscopic curvature, and then incorporated into the LB model as a forcing term.

To conserve the mass and momentum, the perturbation operator should satisfy these constraints:

$$\sum_i (\Omega_i^k)^{(2)} = 0, \quad (15)$$

$$\sum_i (\Omega_i^k)^{(2)} \mathbf{e}_i = 0. \quad (16)$$

Using the Chapman-Enskog multiscale analysis, Eq. (1) can be reduced to the NSEs in the low-frequency, long-wavelength limit with Eqs. (8), (15), and (16). The resulting equations are [43]

$$\partial_t \rho + \nabla \cdot (\rho \mathbf{u}) = 0, \quad (17)$$

$$\partial_t (\rho \mathbf{u}) + \nabla \cdot (\rho \mathbf{u} \mathbf{u}) = -\nabla p + \nabla \cdot [\rho \nu (\nabla \mathbf{u} + \nabla \mathbf{u}^T)] + \nabla \cdot \mathbf{S}, \quad (18)$$

where $p = \sum_k p_k$ is the pressure and $\nu = \frac{1}{3} c^2 (\tau - \frac{1}{2}) \delta_t$ is the kinematic viscosity of the color-blind fluid. The final term in the momentum equation, i.e., $\nabla \cdot \mathbf{S}$, arises from the perturbation operator, and \mathbf{S} is given by

$$\mathbf{S} = -\tau \delta_t \sum_i \Omega_i^{(2)} \mathbf{e}_i \otimes \mathbf{e}_i, \quad (19)$$

where $\Omega_i^{(2)} = \sum_k (\Omega_i^k)^{(2)}$.

It is well known that the expression for the stress jump across the interface is given by

$$\mathbf{T}^R \cdot \mathbf{n} - \mathbf{T}^B \cdot \mathbf{n} = -\nabla \cdot [\sigma (\mathbf{I} - \mathbf{n} \otimes \mathbf{n})], \quad (20)$$

where \mathbf{I} is the second-order identity tensor, $\mathbf{T} = -p\mathbf{I} + \rho \nu (\nabla \mathbf{u} + \nabla \mathbf{u}^T)$ is the stress tensor with the superscript R (B) denoting the red (blue) side of the interface, σ is the interfacial tension, and \mathbf{n} is the interfacial unit normal vector.

In order to induce the local stress jump across the interface, i.e., Eq. (20), a volume-distributed interfacial force $\mathbf{F}(\mathbf{x}, t)$ should be added in the momentum equation as an additional body force. The interfacial force is

$$\mathbf{F}(\mathbf{x}, t) = \nabla \cdot [\sigma (\mathbf{I} - \mathbf{n} \otimes \mathbf{n}) \delta_\Sigma], \quad (21)$$

where δ_Σ is the Dirac delta function used to localize the force explicitly at the interface. The unit normal vector and the Dirac delta function are determined by the gradient of the phase field $\nabla \rho^N$,

$$\mathbf{n} = \frac{\nabla \rho^N}{|\nabla \rho^N|}, \quad \delta_\Sigma = \frac{1}{2} |\nabla \rho^N|. \quad (22)$$

Substitution of Eq. (22) into Eq. (21) yields

$$\mathbf{F}(\mathbf{x}, t) = \nabla \cdot \left[\frac{\sigma}{2|\nabla \rho^N|} (|\nabla \rho^N|^2 \mathbf{I} - \nabla \rho^N \otimes \nabla \rho^N) \right]. \quad (23)$$

Since the perturbation operator is responsible for generating the interfacial tension, the term $\nabla \cdot \mathbf{S}$ in Eq. (18) should be equal to the interfacial force \mathbf{F} , which is derived based on the CSF concept and given by Eq. (23), i.e.,

$$\nabla \cdot \mathbf{S} = \nabla \cdot \left[\frac{\sigma}{2|\nabla \rho^N|} (|\nabla \rho^N|^2 \mathbf{I} - \nabla \rho^N \otimes \nabla \rho^N) \right], \quad (24)$$

or

$$\begin{aligned} \mathbf{S} &= -\tau \delta_t \sum_i \Omega_i^{(2)} \mathbf{e}_i \otimes \mathbf{e}_i \\ &= \frac{\sigma}{2|\nabla \rho^N|} (|\nabla \rho^N|^2 \mathbf{I} - \nabla \rho^N \otimes \nabla \rho^N). \end{aligned} \quad (25)$$

As in Ref. [43], the perturbation operator is chosen to take the form

$$(\Omega_i^k)^{(2)} = \frac{A_k}{2} |\nabla \rho^N| \left[w_i \frac{(\mathbf{e}_i \cdot \nabla \rho^N)^2}{|\nabla \rho^N|^2} - B_i \right]. \quad (26)$$

Substituting Eq. (26) into Eqs. (15), (16), and (25), we obtain

$$\sigma = \frac{2}{9} (A_R + A_B) \tau c^4 \delta_t, \quad (27)$$

$$\sum_i B_i = \frac{1}{3} c^2, \quad \sum_i B_i \mathbf{e}_i = 0, \quad \sum_i B_i \mathbf{e}_i \mathbf{e}_i = \frac{1}{3} c^4 \mathbf{I}. \quad (28)$$

Equation (27) suggests that we can control the interfacial tension through the parameters A_R and A_B . It can be easily justified that the following solutions for B_i satisfy Eq. (28):

$$\begin{aligned} B_0 &= -\frac{2 + 2\chi}{3\chi + 12} c^2, \quad B_{1-6} = \frac{\chi}{6\chi + 24} c^2, \\ B_{7-18} &= \frac{1}{6\chi + 24} c^2, \end{aligned} \quad (29)$$

where χ is a free parameter. For the sake of simplicity, we choose $\chi = 2$ and $\delta_x = \delta_t = 1$ in this study, so that $B_0 = -1/3$, $B_{1-6} = 1/18$, and $B_{7-18} = 1/36$. Without losing generality, we also assume $A_R = A_B = A$, so that Eq. (27) can be written as

$$\sigma = \frac{4}{9} A \tau. \quad (30)$$

With these parameters and assumptions given above, the present perturbation operator obtained through the CSF concept is formally similar to the interfacial-force-related term, i.e., Eqs. (15) and (16) in Ref. [49], but their theoretical basis is totally different. In Ref. [49] the interfacial tension is modeled based on a diffuse-interface theory, in which the parameter A is not only a function of the interfacial tension σ , but also a function of the color or density gradient. More importantly, the interfacial tension is also related to the interface thickness, which is an unknown parameter in Ref. [49]. Therefore, the theoretical expression for the interfacial tension cannot be obtained analytically. In addition, the interfacial-force-related term cannot be used to model a binary fluid with equal densities because the density of the mixture is used to distinguish different fluids. Finally, it should be noted that CSF and diffuse-interface theory both are popular techniques for modeling the interfacial tension force in the traditional computational fluid dynamics (CFD) field. The former is widely used in the VOF and level set methods, while the latter is mainly used in phase field models.

Extending the work of Grunau *et al.* [26] to the D3Q19 lattice, Tölke *et al.* [44] proposed a perturbation operator given by

$$(\Omega_i^k)^{(2)} = A |\mathbf{C}| \left[\frac{(\mathbf{e}_i \cdot \mathbf{C})^2}{|\mathbf{C}|^2} - \frac{5}{9} \right], \quad (31)$$

where \mathbf{C} is the color gradient, which plays an equivalent role to the gradient of the phase field. It is easily found that Eq. (31) satisfies the constraints of Eqs. (15) and (16). However, it gives the tensor \mathbf{S} in the form of

$$\mathbf{S} = \frac{16A\tau\delta_t}{|\mathbf{C}|} \begin{pmatrix} \frac{7|\mathbf{C}|^2 - 27C_x^2}{36} & -C_x C_y & -C_x C_z \\ -C_x C_y & \frac{7|\mathbf{C}|^2 - 27C_y^2}{36} & -C_y C_z \\ -C_x C_z & -C_y C_z & \frac{7|\mathbf{C}|^2 - 27C_z^2}{36} \end{pmatrix}, \quad (32)$$

which cannot be written in the form of Eq. (25). Therefore, the perturbation operator defined by Eq. (31) cannot recover the correct interfacial force term in the NSEs.

The calculation of partial derivatives is required to evaluate the local gradient of the phase field. To minimize the discretization error, these derivatives are calculated using the fourth-order-accurate isotropic finite difference:

$$\frac{\partial \rho^N(\mathbf{x})}{\partial x_\alpha} = \frac{3}{c^2} \sum_i w_i \rho^N(\mathbf{x} + \mathbf{e}_i) e_{i\alpha}, \quad (33)$$

which also contributes enhanced numerical stability [50].

Although the perturbation operator generates interfacial tension, it does not guarantee the immiscibility of both fluids. To promote phase segregation and maintain the interface, the recoloring operator is applied, which enables the interface to be sharp, and at the same time prevents the two fluids from

mixing with each other. In the original recoloring algorithm, the colors are demixed by maximizing the work done by the color gradient (i.e., $\nabla \rho$) against the color flux $\mathbf{q}(\mathbf{x})$, which is defined by

$$\mathbf{q}(\mathbf{x}) = \sum_i [f_i^R(\mathbf{x}) - f_i^B(\mathbf{x})] \mathbf{e}_i. \quad (34)$$

However, when applied to creeping flows, this recoloring algorithm can produce lattice pinning, a phenomenon where the interface can be pinned or attached to the simulation lattice, rendering an effective loss of Galilean invariance [41]. It was also identified that there is an increasing tendency for lattice pinning as both the capillary and Reynolds numbers decrease [45]. We replace the original recoloring algorithm by an antidiffusion scheme proposed by Latva-Kokko and Rothman [41], which can solve the lattice pinning problem and create a symmetric distribution of particles around the interface so that the spurious velocities can be further reduced. Following their method, the recoloring operators for the red and blue fluids are defined by

$$(\Omega_i^R)^{(3)}(f_i^R) = \frac{\rho_R}{\rho} f_i^* + \beta \frac{\rho_R \rho_B}{\rho^2} \cos(\varphi_i) f_i^{\text{eq}}|_{\mathbf{u}=\mathbf{0}}, \quad (35)$$

$$(\Omega_i^B)^{(3)}(f_i^B) = \frac{\rho_B}{\rho} f_i^* - \beta \frac{\rho_R \rho_B}{\rho^2} \cos(\varphi_i) f_i^{\text{eq}}|_{\mathbf{u}=\mathbf{0}}, \quad (36)$$

where f_i^* denotes the postperturbation, pre-segregation value of the total particle distribution function along the i th lattice direction, and $f_i^{\text{eq}} = \sum_k f_i^{k,\text{eq}}$ is the total equilibrium distribution function. β is the segregation parameter related to the interface thickness, and its value must be between 0 and 1 to ensure positive particle distribution functions. φ is the angle between the phase field gradient $\nabla \rho^N$ and the lattice vector \mathbf{e}_i , which is defined by

$$\cos(\varphi_i) = \frac{\mathbf{e}_i \cdot \nabla \rho^N}{|\mathbf{e}_i| |\nabla \rho^N|}. \quad (37)$$

III. NUMERICAL RESULTS AND DISCUSSION

The usefulness and accuracy of the improved LB model will be verified and examined by three numerical examples, specifically, a test of the Laplace law, droplet deformation and breakup in simple shear flow, and a single bubble rising in viscous liquids at various flow conditions. In the latter two examples, our simulation results will be compared with theoretical and experimental findings.

A. Test of the Laplace law with a stationary bubble

The first test problem represents a traditional benchmark for a two-phase flow model. It consists of a blue spherical bubble initially located at the center of a red fluid domain with $65 \times 65 \times 65$ lattice cells. Periodic boundary conditions are imposed at all boundaries. According to the Laplace law, when the system reaches the equilibrium state, the pressure difference across the bubble interface Δp is related to the interfacial tension σ as

$$\Delta p = \frac{2\sigma}{R}, \quad (38)$$

where R is the radius of the bubble. Given the pressure difference and the radius from the simulation, one can calculate

TABLE I. Stationary bubble test in a computational domain of $65 \times 65 \times 65$ lattice cells. Note that we set $\rho_B = 1.0$ and $\alpha_B = 1/5$ for all the stationary bubble simulations.

ρ_R	α_R	σ_{theory}	$\beta = 0.7$			$\beta = 1$			$\sigma_{\text{Laplace [44]}}$	$E\%$
			σ_{Laplace}	$E\%$	$ \mathbf{u} _{\text{max}}$	σ_{Laplace}	$E\%$	$ \mathbf{u} _{\text{max}}$		
1	$\frac{1}{5}$	0.024	0.0243	1.30	5.0×10^{-4}	0.0242	0.83	8.8×10^{-4}	0.0237	1.3
1	$\frac{1}{5}$	0.096	0.0972	1.28	1.9×10^{-3}	0.0967	0.76	3.5×10^{-3}	0.0956	0.4
1	$\frac{1}{5}$	0.24	0.2429	1.21	4.7×10^{-3}	0.2417	0.73	8.6×10^{-3}	0.224	6.6
2	$\frac{3}{5}$	0.108	0.1097	1.58	1.4×10^{-3}	0.1089	0.84	2.4×10^{-3}	0.1067	1.2
10	$\frac{23}{25}$	0.132	0.1346	1.95	1.2×10^{-3}	0.1333	1.00	2.0×10^{-3}	0.1264	4.2
30	$\frac{73}{75}$	0.1116	0.1140	2.12	1.0×10^{-3}	0.1126	0.92	1.8×10^{-3}	0.0966	13.4
100	$\frac{124}{125}$	0.1	0.1029	2.83	9.0×10^{-4}	0.1012	1.16	1.7×10^{-3}	–	–
1000	$\frac{1249}{1250}$	0.1	0.1038	3.65	7.2×10^{-4}	0.1016	1.58	1.3×10^{-3}	–	–

the interfacial tension σ_{Laplace} using Eq. (38) and compare it with the theoretical value σ_{theory} , which is set by specifying A based on Eq. (30). The radius of the bubble is 16 lattice units, and the relaxation time τ is set to unity. Table I gives the simulation results for the segregation parameter $\beta = 0.7$ and 1 at several different interfacial tensions and density ratios. A numerical artifact observed in many numerical methods is the presence of spurious velocities at the phase interface. This is also true in our case. For the sake of comparison, Table I also gives the magnitude of the maximum spurious velocities for each β . It can be clearly seen that the calculated interfacial tensions (σ_{Laplace}) agree well with the theoretical ones (σ_{theory}) for both $\beta = 0.7$ and 1. However, changing β has opposite effects on the accuracy of the interfacial tension and the magnitude of the maximum spurious velocities. Specifically, $\beta = 1$ produces the more accurate interfacial tension while $\beta = 0.7$ generates lower spurious velocities. Finally, in order to further show the superiority of the present model, the simulation results of Tölke *et al.* [44] are listed in Table I as well. Generally, the interfacial tension obtained by the present model has higher numerical accuracy especially at high density ratios. It is therefore expected that the present model is a better candidate for the simulation of binary fluids with different densities. Note that the error for the interfacial tension (which is calculated by $E\% = \frac{|\sigma_{\text{theory}} - \sigma_{\text{Laplace}}|}{\sigma_{\text{theory}}} \times 100\%$) changes slightly as the interfacial tension or the density ratio increases, which is different from the observation of Tölke *et al.* [44].

To simulate large-scale multiphase flows in an industrial process, computational efficiency is one of the most important factors determining the applicability of a model. As we stated in the Introduction, most of the currently available LB high-density-ratio multiphase models suffer from high computing costs. Here we present a comparison of the required computational time between the present model and the phase field model recently proposed by Lee and Liu [37]. The phase field model is also used to simulate the stationary bubble case with the density ratio of 100. The serial codes for the two models are both run on a personal workstation equipped with eight Intel Xeon E5630 2.53 GHz cores and 6 Gbytes RAM. For each 1000 lattice time steps, the required CPU time is 700.99 s for the present model and 1558.23 s for the phase field model, respectively. In addition, the two models need different time steps to achieve the same stopping criterion. For

example, the stopping criterion is commonly chosen as

$$\frac{\sum_{\mathbf{x}} [\rho^N(\mathbf{x}, t) - \rho^N(\mathbf{x}, t - 100)]^2}{\sum_{\mathbf{x}} [\rho^N(\mathbf{x}, t)]^2} < 10^{-10}. \quad (39)$$

Note that the phase field ρ^N is the local composition of one of the two phases in the phase field model. We find that the present model with $\beta = 0.7$ ($\beta = 1.0$) needs 5400 (2900) lattice time steps to achieve the above-mentioned stopping criterion, while the phase field model with the interface thickness $\xi = 5$ (which is defined in Ref. [37]) needs 127 800 lattice time steps. Obviously, the present model has much higher computational efficiency compared to the phase field model of Lee and Liu [37].

B. Droplet deformation and breakup in simple shear flow

Taylor deformation is often used to assess whether a multiphase model is able to simulate dynamic problems. A droplet is placed between two parallel plates which are moving in opposite directions to obtain a linear shear in the Stokes flow regime (i.e., small Reynolds number). Droplet deformation is studied as a function of the shear rate, which is expressed by the capillary number. The definitions of the Reynolds number and the capillary number are

$$\text{Re} = \frac{\gamma R^2 \rho}{\eta}, \quad \text{Ca} = \frac{\gamma R \eta}{\sigma}, \quad (40)$$

where $\gamma = U/H$ is the shear rate with U being the velocity of the moving plate and H being the half channel height; R is the initial radius of the droplet; $\eta = \rho \nu$ is the dynamic viscosity. For this case, we assume that both fluids have equal density and viscosity. The simulations are first run at $\text{Re} = 0.1$ for a spherical droplet with the radius of ten lattice cells in a system of $100 \times 50 \times 50$ lattice cells. At steady state, the droplet is assumed to be ellipsoidal, which is usually characterized by the deformation parameter D_f , defined as

$$D_f = \frac{a - b}{a + b}, \quad (41)$$

where a and b are the lengths of the major and minor axes of the deformed droplet, respectively. For a droplet in the Stokes regime with a low Ca , D_f follows the Taylor relation as [51]

$$D_f = (35/32)\text{Ca}. \quad (42)$$

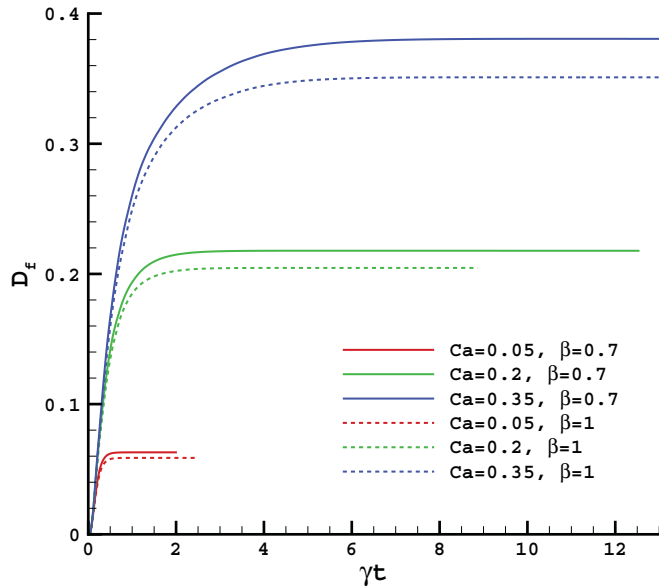


FIG. 1. (Color online) Time evolution of the Taylor deformation parameter for $\beta = \{0.7, 1\}$ at $Ca = \{0.05, 0.2, 0.35\}$ and $Re = 0.1$.

A series of numerical simulations are performed with $\beta = \{0.7, 1\}$ and Ca varying from 0.05 to 0.35. Figure 1 shows the time evolution of the Taylor deformation parameter for different Ca and β . It can be observed that the droplet can evolve to a steady state for both $\beta = 0.7$ and $\beta = 1$. However, a large β (i.e., a small interface thickness) usually produces a small droplet deformation at a fixed Ca . This can be also clearly seen in Fig. 2, which plots the Taylor deformation parameter as a function of the capillary number at $Re = 0.1$. Obviously, the LB simulations with $\beta = 0.7$ are in good agreement with the theoretical Taylor relation. In addition, a recent theoretical analysis and numerical experiment also demonstrated that $\beta <$

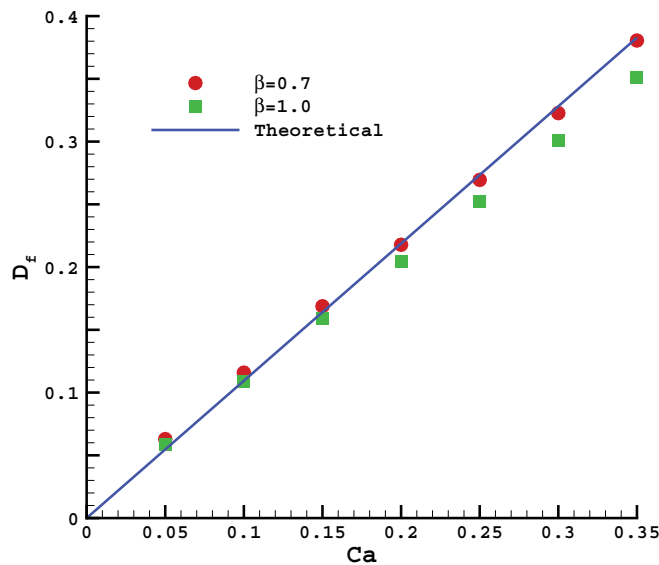


FIG. 2. (Color online) Taylor deformation parameter D_f as a function of the capillary number at $Re = 0.1$. The solid line is the theoretical Taylor relation given by Eq. (42).

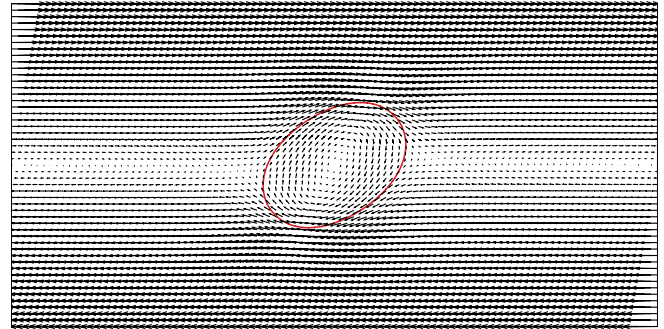


FIG. 3. (Color online) Velocity field of the droplet deformation in the x - z meridian plane at $Ca = 0.2$ and $Re = 0.1$.

0.71 is necessary to obtain a stable and continuum interface for a stationary droplet [46]. Therefore, we will use $\beta = 0.7$ in the following simulations in order to reproduce the correct droplet dynamic behavior.

A recent numerical study [42] observed that, when the original color-fluid model of Gunstensen *et al.* is applied for droplet deformation in the simple shear flow with small Reynolds number and capillary number, large spurious velocities can induce unphysical eddies and large variation in velocity near the droplet interface, resulting in an incorrect deformation of the droplet. Figure 3 shows the velocity field around the deformed droplet in the x - z meridian plane at $Ca = 0.2$ and $Re = 0.1$. Since the present model can effectively suppress the spurious velocities, we can see a smooth velocity field with an elliptical vortex inside the droplet, which is a typical feature of reasonable droplet deformation [52].

Several previous theoretical, experimental, and numerical studies [52–56] have indicated that in the creeping flow regime, when the viscosity ratio of the droplet to the matrix fluid λ is less than 4, there is a “critical capillary number” Ca_c , above which the droplet continues to deform without reaching a steady shape, and this finally leads to droplet breakup. The critical capillary number for droplet breakup in shear flow is lowest for λ roughly around 0.6 [53], and its value ($Ca_c \approx 0.4$) is slightly less than the case for $\lambda = 1$, where $Ca_c \approx 0.41$ [57]. The critical capillary number was numerically and experimentally found to be a function of the geometry confinement ratio R/H for $\lambda = 1$ [58–60]. Due to an unidentified systematic error, Janssen *et al.* [60] found in all data sets that the experiments gave a slightly higher critical capillary number, but trends were found to be identical. A minimum in Ca_c is reached at a geometry confinement ratio of approximately 0.5 with its value equal to 0.37 and 0.41 for the simulations and experiments, respectively. Li *et al.* [52] used the volume-of-fluid method to investigate the droplet breakup in simple shear flows and found that, when the geometry confinement ratio is large ($R/H = 0.5$), no steady deformation is obtained for $Ca = 0.4$, implying that $Ca_c < 0.4$. On the other hand, for small geometry confinement ratio ($R/H = 0.125$), a steady deformation is obtained for $Ca = 0.4$ and the flow becomes unsteady for $Ca = 0.42$. They concluded that the close proximity of the two moving plates reduces the critical capillary number.

The present model is also used to predict the critical capillary number. To examine more carefully the deformation

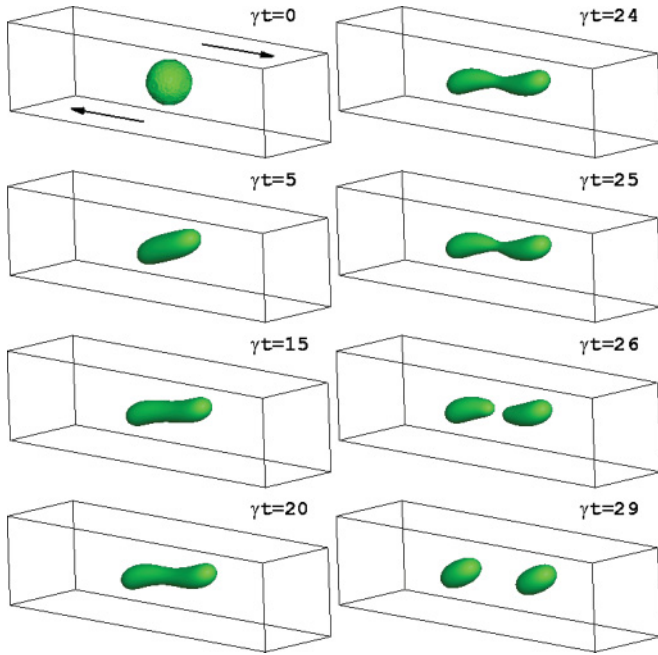


FIG. 4. (Color online) Evolution of droplet shape for $Ca = 0.4$, $Re = 0.1$, and $R/H = 0.5$ in a computational domain of $240 \times 60 \times 60$ lattice cells.

and breakup processes, we have done the calculation in a $240 \times 60 \times 60$ lattice domain with the droplet radius $R = 15$ lattice units such that the geometry confinement ratio $R/H = 0.5$. The Reynolds number is still kept at $Re = 0.1$. We observe that the droplet can evolve to a steady shape for $Ca = 0.35$ (at steady state $D_f = 0.543$), whereas the breakup occurs for $Ca = 0.4$. It is evident that the critical capillary number lies between 0.35 and 0.4, which is in agreement with previous numerical results obtained with the boundary integral method [60] and the volume-of-fluid method [52]. Figure 4 shows the evolution of droplet shape for $Ca = 0.4$, $Re = 0.1$, and $R/H = 0.5$. The droplet deforms continuously and eventually breaks up into two equal parts, which is referred to as binary breakup. The competition between the externally imposed shear flow and the interfacial-tension-driven flow is obvious in this figure. Initially, the most noticeable motion is the elongation of the droplet, stretched by the viscous shear stresses from the external flow ($\gamma t = 0, 5$, and 15). At time $\gamma t = 20$, we can clearly see that a waist is formed near the center of the droplet, and the droplet continually thins. The droplet begins to lengthen slowly and a visible neck is formed near the center of the droplet ($\gamma t = 24$). The neck continues to thin ($\gamma t = 25$) and eventually pinches off, leading to formation of two equal-sized droplets ($\gamma t = 26$ and 29).

Next, we investigate the effect of Reynolds number on the droplet breakup. We focus on the case $Ca = 0.4$ and $R/H = 0.5$, and increase the Reynolds number from 0.1 to 2, i.e., $Re = \{0.1, 0.5, 1, 2\}$. For the former three cases, the computational domain is chosen as $240 \times 60 \times 60$ lattice cells, while for the case of $Re = 2$ the computational domain is increased to $360 \times 60 \times 60$ lattice cells in consideration of the long stretching in the x direction. When the Reynolds number is increased from 0.1 to 0.5, one can observe in Fig. 5 that the droplet is elongated and breakup occurs at

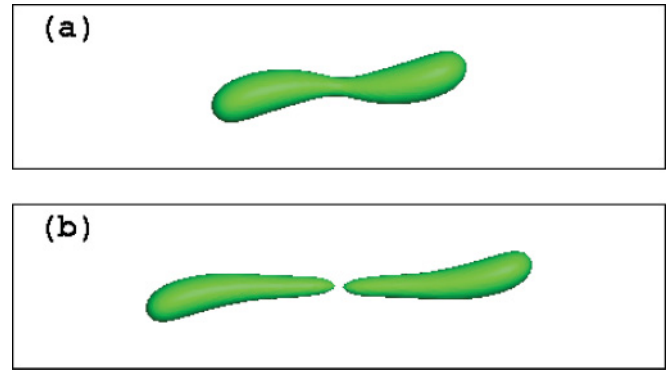


FIG. 5. (Color online) Comparison of the droplet shape, viewed from the front of the computational domain, for (a) $Re = 0.1$ and (b) $Re = 0.5$ at $Ca = 0.4$ and $R/H = 0.5$. The time is taken at $\gamma t = 25$ and 23 , respectively.

an earlier time, although both cases exhibit binary breakup. It is therefore expected that increasing the Reynolds number can increase the droplet deformation and promote the droplet breakup, which is consistent with the finding of Li *et al.* [52]. When the Reynolds number is increased to 1, the droplet breaks up into three parts (i.e., ternary breakup) with two daughter droplets having slightly larger size (see Fig. 6). If we continue to increase the Reynolds number to 2, the droplet will disintegrate into more daughter droplets. Figure 7 gives the snapshots of droplet breakup for $Ca = 0.4$, $Re = 2$, and $R/H = 0.5$. We can observe that the first four daughter droplets are formed by the end pinching ($\gamma t = 24$ and 25). Next, the intermediate ligament breaks into two parts, which then retract to a “dumbbell” shape ($\gamma t = 27$) and eventually stabilize to an ellipsoid shape ($\gamma t = 34$). By comparing the simulation results for different Re , we can obtain the result that

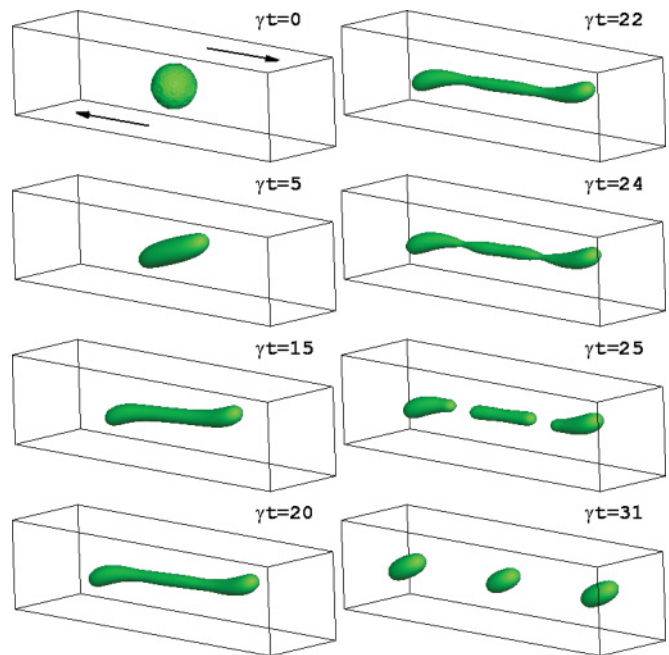


FIG. 6. (Color online) Evolution of droplet shape for $Ca = 0.4$, $Re = 1$, and $R/H = 0.5$ in a computational domain of $240 \times 60 \times 60$ lattice cells.

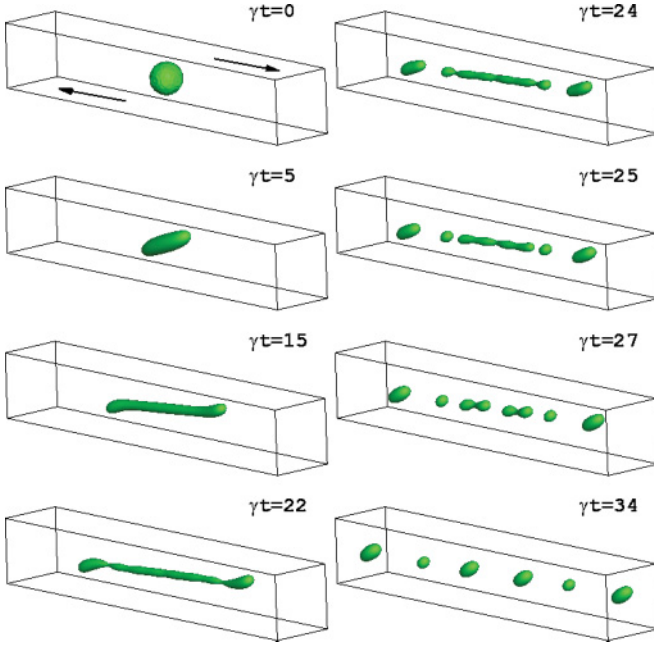


FIG. 7. (Color online) Evolution of droplet shape for $Ca = 0.4$, $Re = 2$, and $R/H = 0.5$ in a computational domain of $360 \times 60 \times 60$ lattice cells.

the droplet breakup becomes increasingly unstable and the end pinching becomes increasingly pronounced, disintegrating the droplet as Re increases.

C. Single bubble rising in viscous liquids

Bubble rise subject to gravity is one of the most common gas-liquid flow phenomena. Understanding bubble dynamics is of great importance for the design and operation of industrial applications such as liquid rocket motors and blood-pumping machines. As a fundamental subject of fluid mechanics, the dynamic behavior of a gas bubble rising in a viscous liquid has been investigated both numerically and experimentally by numerous authors for many years. A detailed review of experimental studies and correlations was provided by Clift *et al.* [61]. Later, Bhaga and Weber [62] presented a more comprehensive study, in which shape regimes and bubble terminal rise velocity are correlated on the basis of experimental data. Different shapes of bubbles, namely, spherical, oblate ellipsoidal, oblate ellipsoidal cap, and skirted bubbles, can be observed in the experiments [62], and strongly depend on the values of four important dimensionless parameters. These dimensionless parameters are the viscosity ratio λ , the Eötvös number Eo , the Morton number Mo , and the Reynolds number Re , which are defined as

$$\lambda = \frac{\eta_g}{\eta_l}, \quad Eo = \frac{g \Delta \rho D^2}{\sigma}, \quad Mo = \frac{g \Delta \rho \eta_l^4}{\sigma^3 \rho_l^2}, \quad Re = \frac{\rho_l U_t D}{\eta_l}, \quad (43)$$

where η_l and η_g are the dynamic viscosities of the liquid and gas phases, $\Delta \rho = \rho_l - \rho_g$ is the density difference between liquid and gas, D is the bubble diameter, g is the gravitational acceleration, and U_t is the terminal velocity of the rising bubble.

In the present study $\rho_l = 2$ and $\rho_g = 0.4$ are chosen, and the kinematic viscosities for both phases are kept equal so that $\lambda = \frac{\rho_g}{\rho_l} = \frac{1}{5}$. The bubble diameter is fixed at $D = 24$ lattices. The buoyancy force \mathbf{G} is defined in such a way that it affects only the gas, equivalent to $\mathbf{G} = -(\rho - \rho_l)g\mathbf{i}_z$, where \mathbf{i}_z represents a unit vector pointing in the positive z direction. The buoyancy force is introduced into the LBM through a forcing term given by Guo *et al.* [63]. Simulations are performed in an enclosed cubic domain and bounceback [64] is used on all boundaries in order to obtain no-slip boundary conditions. To reduce the wall viscous effect, the lateral domain sizes of $4D$ are selected, since they provide a final bubble shape very close to that in a larger domain and the difference in terminal velocity is less than 10% [65]. The influence of the vertical domain size is different in each case, since the bubble motion depends on the magnitude of Re . For cases of $Re \sim 1$, the vertical size of $4D$ is sufficient. However, for $Re \sim 100$ the vertical size has to be as high as $9D$ [65,66]. Therefore, in what follows, we will use the computational domain $L_x \times L_y \times L_z = 4D \times 4D \times 14D$.

First, the influence of Morton number on the bubble motion is investigated at a fixed $Eo = 32$. The Morton number is varied from 10^4 to 0.1 . Figure 8 shows the evolution of the bubble velocity and the instantaneous Reynolds number (which is defined by the bubble velocity u_d as $Re^* = \frac{\rho_l u_d D}{\eta_l}$) with time for a rising bubble at $Mo = \{10^4, 10^3, 10^2, 1, 10^{-1}\}$. The bubble velocity and time have been normalized as $u_d^* = \frac{u_d}{\sqrt{gD}}$ and $t^* = t\sqrt{\frac{g}{D}}$. It can be observed that the bubble motion can evolve to a steady state for all the Morton numbers. However, we also notice that the Morton number has different effects on the evolution of bubble velocity: at large Mo the bubble velocity quickly increases to a constant, whereas at small Mo the bubble velocity first increases to a peak value and then decreases until a steady terminal velocity is reached. The overshoot in velocity becomes increasingly evident with an increase in Morton number, indicating that the bubble motion has a tendency to increasing instability. In addition, we can find in Fig. 8 that the terminal velocity (or the Reynolds number) increases as Mo decreases, consistent with previous experimental observations [61,62]. Figure 9 gives the final shapes for the rising bubble for various Mo at $Eo = 32$. Note that the bubble is spherical for the case of $Mo = 10^4$, which is not shown in this figure. We can clearly see that, as Mo increases, the bubble shape successively undergoes three different regimes, namely, spherical, oblate ellipsoid, and oblate ellipsoidal cap regimes. The increase in bubble deformation is attributed to the fact that the interfacial tension, which prevents the bubble deformation, becomes less important in comparison with the buoyancy with the increase in Mo .

Next, the accuracy of the numerical results is examined by comparing with experimental correlations and theoretical predictions. The parameters used in our simulations are summarized in Table II. For each case, the interfacial tension, Mo , and Eo are initially given; g and τ can be easily calculated by Eqs. (43) and (12). It can be seen that a broad range of τ is included in our simulations (0.54–1.73), indicating that the present model has good numerical stability. When the bubble motion reaches steady state, the obtained terminal velocity U_t is used to calculate the Reynolds number, which is also given

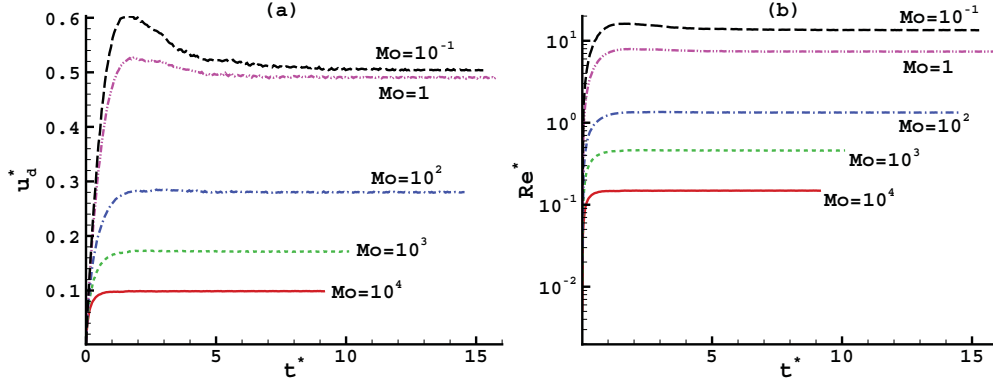


FIG. 8. (Color online) Variation of (a) the normalized bubble velocity and (b) the instantaneous Reynolds number with time for different Morton numbers at $Eo = 32$.

in Table II. Figure 10 gives several typical bubble shapes in the x - z meridian plane with the corresponding case number shown on the left side of each deformed bubble. Note that Fig. 10 does not show the bubble shapes for the cases (f)–(i) because they have been shown previously in Fig. 9. As can

be seen from Figs. 9 and 10, our numerical simulations have covered a wide range of bubble shape regimes.

During the process of bubble rise, there are two main forces acting on the bubble: buoyancy and drag. Buoyancy acts to drive the bubble motion while drag opposes the motion. When these two forces are balanced, the bubble motion reaches a steady state and the bubble rises at a constant velocity (i.e., the terminal velocity). The drag coefficient can be obtained from the force balance and is given by

$$C_D = \frac{4\Delta\rho g D}{3U_T^2 \rho_l}. \quad (44)$$

The calculated drag coefficients have been compared to the experimental correlation of Bhaga and Weber [62], in which the drag coefficient for fluid systems with large values of Morton number ($Mo > 4 \times 10^{-3}$) is said to obey the relationship

$$C_D = \left[(2.67)^{0.9} + \left(\frac{16}{Re} \right)^{0.9} \right]^{1/0.9}. \quad (45)$$

TABLE II. Parameters for single bubble rising using the LBM.

Case	σ	Eo	Mo	Re
(a)	2×10^{-2}	1	1×10^{-2}	0.80
(b)	2×10^{-3}	10	5×10^2	0.12
(c)	4×10^{-3}	10	1×10^0	2.26
(d)	4×10^{-3}	10	1×10^{-3}	23.99
(e)	3×10^{-4}	32	1×10^4	0.15
(f)	4×10^{-4}	32	1×10^3	0.46
(g)	1×10^{-3}	32	1×10^2	1.33
(h)	1×10^{-3}	32	1×10^0	7.39
(i)	1×10^{-3}	32	1×10^{-1}	13.47
(j)	5×10^{-5}	100	1×10^5	0.26
(k)	1×10^{-4}	100	1×10^4	0.77
(l)	5×10^{-4}	100	1×10^2	4.90
(m)	1×10^{-3}	100	1×10^0	17.78
(n)	1×10^{-3}	100	1×10^{-1}	33.72
(o)	1×10^{-4}	1000	1×10^6	2.09
(p)	1×10^{-5}	1000	1×10^5	4.79
(q)	1×10^{-4}	1000	1×10^4	9.32
(r)	2×10^{-5}	1000	1×10^3	17.31

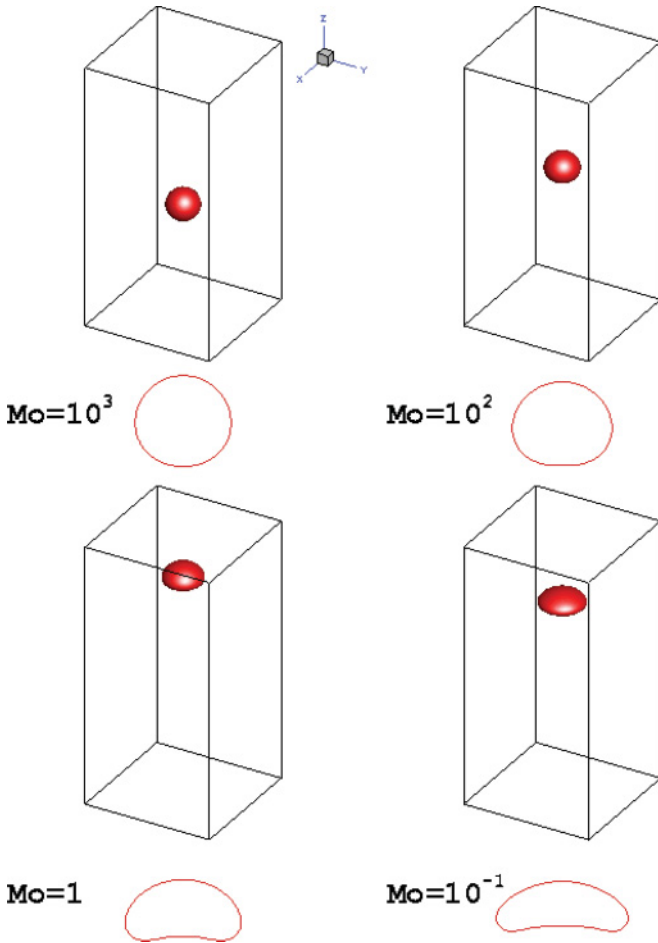


FIG. 9. (Color online) Effect of Mo on the terminal shape of a rising bubble at $Eo = 32$. For each Mo , the upper graph is the three-dimensional simulation result, and the lower one is the corresponding bubble shape in the x - z meridian plane.

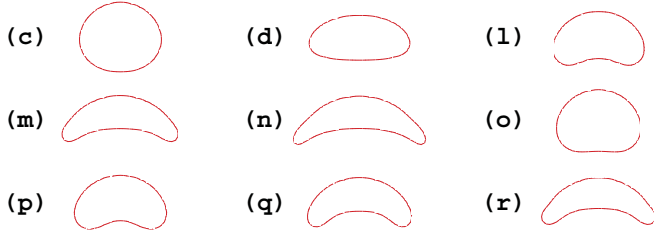


FIG. 10. (Color online) Typical bubble shapes for the cases given in Table II. The case number is shown on the left side of the rising bubble for each case.

The results of the numerical simulations have also been compared to the theoretical prediction of Joseph [67], which was derived based on the theory of viscous potential flow and the information of Davies and Taylor [68] at the asymptotic large-Re limit. The drag coefficient is given as

$$C_D = 0.445 \left(6 + \frac{32}{\text{Re}} \right). \quad (46)$$

These results are shown in Fig. 11. It can be seen that the simulation results are in good agreement with the experimental correlation and theoretical prediction.

In addition to comparing the numerical drag coefficient with the experimental correlation and theoretical prediction, the flow number and the velocity number, which are defined by [69]

$$F = g \left(\frac{D^8 \rho_l^5}{\sigma \eta_l^4} \right)^{1/3}, \quad (47)$$

$$V = U_t \left(\frac{D^2 \rho_l^2}{\sigma \eta_l} \right)^{1/3}, \quad (48)$$

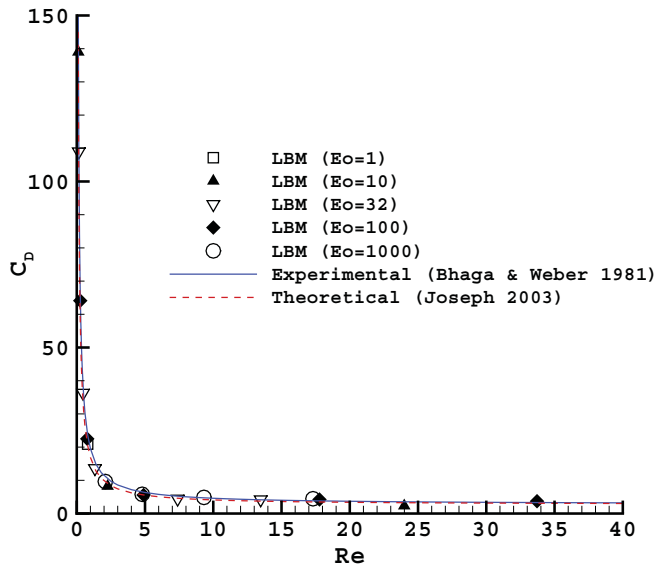


FIG. 11. (Color online) Drag coefficient versus Reynolds number for a rising bubble. The discrete points are obtained from three-dimensional lattice Boltzmann simulations. The dashed and solid lines represent the theoretical solution of Joseph [67] and the experimental correlation of Bhaga and Weber [62], respectively.

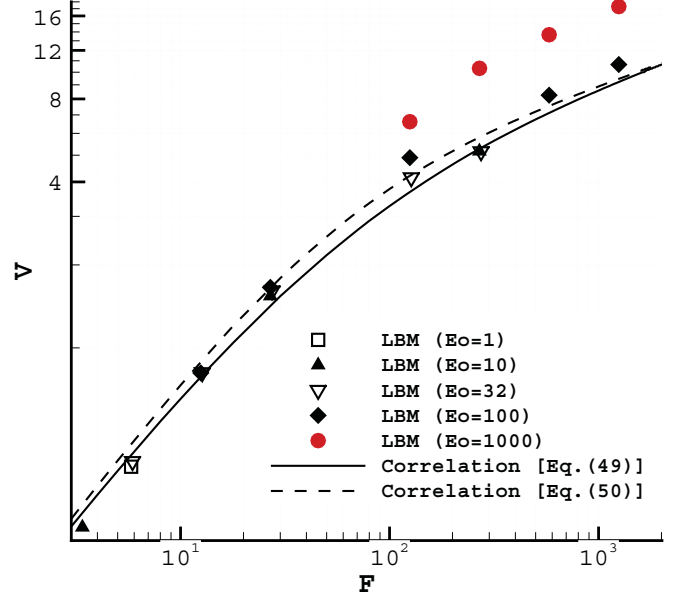


FIG. 12. (Color online) Velocity number versus flow number for a rising bubble. The discrete points are obtained from three-dimensional lattice Boltzmann simulations. The solid and dashed lines represent the experimental correlations of Eq. (49) and Eq. (50), respectively.

are also evaluated and compared to the following empirical correlations [69]:

$$V = \frac{F}{12 + 0.588 F^{0.75}}, \quad (49)$$

$$V = \frac{F}{(12 + 0.0188 F)^{0.75}}, \quad (50)$$

As can be observed in Fig. 12, for $Eo \leq 100$ our LBM results are in satisfactory agreement with the correlations of Eqs. (49) and (50), whereas for the highest Eo , i.e., $Eo = 1000$, there exist large differences between our LBM results and the prediction values. To clarify the cause of the large differences, it is necessary to know the accuracy of our numerical simulations. Fortunately, for a rising bubble in an infinite medium with $Eo > 40$ and $Mo > 200$, the Reynolds number can be obtained analytically through solution of the following equation [61]:

$$2\text{Re}^2 + 6\text{Re} \frac{2 + 3\lambda}{1 + \lambda} - Eo^{3/2} Mo^{-1/2} = 0. \quad (51)$$

From Eq. (51), the theoretical values of the Reynolds number are obtained as 1.89, 4.53, 9.74, and 19.34 for $Mo = 10^6, 10^5, 10^4,$ and 10^3 at $Eo = 1000$. On the other hand, as shown in Table II, the simulation results for the Reynolds number are 2.09, 4.79, 9.32, and 17.31 for $Mo = 10^6, 10^5, 10^4,$ and 10^3 at $Eo = 1000$. Obviously, our simulation results agree well with the theoretical solutions, indicating that our numerical simulations can provide satisfactory accuracy. Based on the big differences shown in Fig. 12, we can conclude that the correlations of Eqs. (49) and (50) are not applicable to describe a rising bubble with very high Eo .

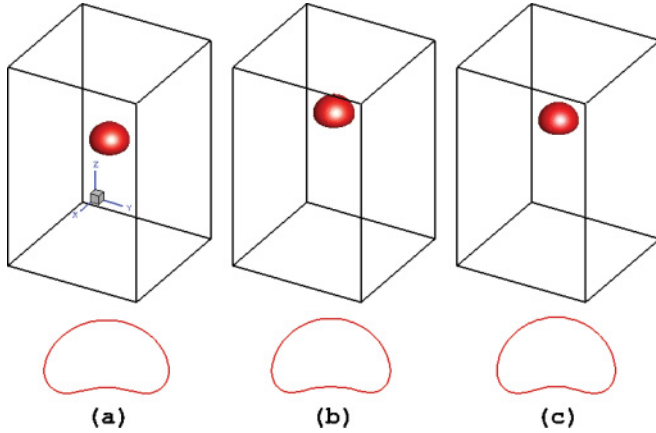


FIG. 13. (Color online) Terminal shapes of rising bubble at $Mo = 266$ and $Eo = 116$ for the density ratio of (a) 10, (b) 50 and (c) 80. For each density ratio, the upper graph is the three-dimensional simulation result, and the lower one is the corresponding bubble shape in $x - z$ meridian plane.

To further investigate the capability of the present model in simulating multiphase flows with high density ratio, we simulate a bubble rising under buoyancy for $Mo = 266$ and $Eo = 116$ with the density ratios of 10, 50, and 80. The liquid density is still kept at 2, and the gas density is varied to obtain different density ratios. We also choose the interfacial tension $\sigma = 6 \times 10^{-5}$, and the kinematic viscosities for both fluids are kept equal in these three simulations. Figure 13 gives the final shapes for a rising bubble at $Mo = 266$ and $Eo = 116$ for the density ratios of (a) 10, (b) 50, and (c) 80. We can see that the bubble shape does not change much with an increase in density ratio. This may be attributed to the small variation in Reynolds number when the density ratio is increased. For the density ratio $\lambda = 10, 50,$ and 80 , the simulation results for the Reynolds number are 3.88, 4.06, and 4.17, respectively, indicating good agreement with the theoretical values (which are 3.8, 3.86, and 3.87) obtained by Eq. (51). However, numerical instability is observed when the density ratio is increased to 100. The numerical instability results from the negative density of the gas phase at the interface. Actually, a similar numerical instability is also observed for a single bubble rising in the phase field model of Lee and Liu [37] when the density ratio is increased to 100 or higher. Therefore, an artificial pressure gradient term is introduced to avoid a negative value of the composition [65]. However, the physical meaning of this artificial pressure gradient term is still unclear.

IV. CONCLUSIONS

In this paper, a lattice Boltzmann color-fluid model is proposed to simulate three-dimensional immiscible binary fluids using a D3Q19 lattice. An equilibrium distribution function and single-relaxation-time collision operator for each fluid are provided, allowing each fluid to have its own density and viscosity. To recover the correct form of the Navier-Stokes equations, the perturbation operator should satisfy mass conservation, momentum conservation, and an additional constraint, which is responsible for generating

the interfacial tension. With the concept of a continuum surface force to model the interfacial tension, we have derived a generalized expression for the perturbation operator. In addition, a theoretical expression for the interfacial tension parameter is obtained directly without any additional analysis or approximations. A recoloring algorithm proposed by Latva-Kokko and Rothman [41] is applied for separating two fluids, which can overcome “lattice pinning,” a problem that may prevent the interface from moving.

This model is first validated against the Laplace law for the interfacial tension. It is found that the segregation parameter β has an opposite effect on the magnitude of spurious velocities and the accuracy of interfacial tension: a larger β yields a more accurate interfacial tension but larger spurious velocities. This model is then used to simulate single-droplet deformation and breakup under simple shear flow. We investigate the droplet deformation for small capillary numbers in the Stokes flow regime, and find that the numerical results with $\beta = 0.7$ are in excellent agreement with the theoretical Taylor relation, while the numerical simulations with $\beta = 1$ underpredict the deformation. For a geometry confinement ratio $R/H = 0.5$, we find that in the limit of creeping flow the droplet breakup occurs at a critical capillary number $0.35 < Ca_c < 0.4$, consistent with previous numerical simulations and experiments [52,60]. An increase in the Reynolds number can increase the droplet deformation and promote droplet breakup, leading to formation of more small droplets. Finally, this model is applied to simulate buoyancy-driven motion of a single bubble. It is observed that at a fixed Eötvös number an increase in Morton number can enhance the deformation and the terminal velocity of the rising bubble, so that the instability of the bubble is increased. Numerical simulations are carried out with a wide range of Eötvös and Morton numbers, and many bubble shape regimes are observed. The calculated drag coefficient is compared with experimental correlations [62] and theoretical predictions [67], and good agreement is shown. We also compare our numerical results with the correlation of Rodrigue [69], which was obtained using a dimensionless analysis on experimental data from 19 studies. We have demonstrated that this correlation is not applicable for describing rising bubbles with high Eötvös number, although our numerical results are in satisfactory agreement with this correlation for $Eo \leq 100$.

ACKNOWLEDGMENTS

This paper is based upon work supported by the LDRD Program (Grant No. 20100025DR) of the Los Alamos National Laboratory. The authors thank two anonymous referees for their helpful suggestions.

APPENDIX: DERIVATION OF THE NAVIER-STOKES EQUATIONS IN THE SINGLE-PHASE REGION

In each pure fluid, the gradient of the phase field is zero, so the perturbation operator $(\Omega_i^k)^{(2)} = 0$ and the recoloring operator $(\Omega_i^k)^{(3)}$ is a unit operator. The collision operator in Eq. (2) can be simplified as $\Omega_i^k = (\Omega_i^k)^{(1)}$, and one can rewrite

Eq. (1) as

$$f_i^k(\mathbf{x} + \mathbf{e}_i \delta_t, t + \delta_t) = f_i^k(\mathbf{x}, t) - \frac{f_i^k(\mathbf{x}, t) - f_i^{k,\text{eq}}(\mathbf{x}, t)}{\tau_k} \quad (k = R \text{ or } B) \quad (\text{A1})$$

with $f_i^{k,\text{eq}}$ given by Eq. (8). Introducing the Chapman-Enskog expansion

$$f_i^k(\mathbf{x} + \mathbf{e}_i \delta_t, t + \delta_t) = \sum_{n=0}^{\infty} \frac{\epsilon^n}{n!} D_t^n f_i^k(\mathbf{x}, t), \quad (\text{A2})$$

$$f_i^k = \sum_{n=0}^{\infty} \epsilon^n f_i^{k,(n)}, \quad (\text{A3})$$

$$\partial_t = \sum_{n=0}^{\infty} \epsilon^n \partial_{t_n}, \quad (\text{A4})$$

where $\epsilon = \delta_t$ and $D_t \equiv (\partial_t + \mathbf{e}_i \cdot \nabla)$, the following equations are obtained up to second order in the parameter ϵ :

$$O(\epsilon^0): f_i^{k,(0)} = f_i^{k,\text{eq}}, \quad (\text{A5})$$

$$O(\epsilon^1): D_{t_0} f_i^{k,(0)} = -\frac{1}{\tau_k} f_i^{k,(1)}, \quad (\text{A6})$$

$$O(\epsilon^2): \partial_{t_1} f_i^{k,(0)} + \left(1 - \frac{1}{2\tau_k}\right) D_{t_0} f_i^{k,(1)} = -\frac{1}{\tau_k} f_i^{k,(2)}, \quad (\text{A7})$$

where $D_{t_n} \equiv (\partial_{t_n} + \mathbf{e}_i \cdot \nabla)$. Note that one can use the following solvability conditions for $f_i^{k,(n)}$ ($n = 1, 2, \dots$):

$$\sum_i f_i^{k,(n)} = 0, \quad \sum_i f_i^{k,(n)} e_{i\alpha} = 0, \quad (\text{A8})$$

and the conditions for the equilibrium distribution function $f_i^{k,\text{eq}}$ are

$$\begin{aligned} \sum_i f_i^{k,\text{eq}} &= \rho_k, \quad \sum_i f_i^{k,\text{eq}} e_{i\alpha} = \rho_k u_\alpha, \\ \sum_i f_i^{k,\text{eq}} e_{i\alpha} e_{i\beta} &= \rho_k u_\alpha u_\beta + p_k \delta_{\alpha\beta}, \\ \sum_i f_i^{k,\text{eq}} e_{i\alpha} e_{i\beta} e_{i\gamma} &= \frac{1}{3} \rho_k c^2 (u_\alpha \delta_{\beta\gamma} + u_\beta \delta_{\alpha\gamma} + u_\gamma \delta_{\alpha\beta}), \end{aligned} \quad (\text{A9})$$

where p_k is defined by Eq. (10).

The zeroth- and first-order moments of Eq. (A6) lead to

$$\partial_{t_0} \rho_k + \partial_\alpha (\rho_k u_\alpha) = 0, \quad (\text{A10})$$

$$\partial_{t_0} (\rho_k u_\alpha) + \partial_\beta (\rho_k u_\alpha u_\beta + p_k \delta_{\alpha\beta}) = 0. \quad (\text{A11})$$

The moments of Eq. (A7) lead to

$$\partial_{t_1} \rho_k = 0, \quad (\text{A12})$$

$$\partial_{t_1} (\rho_k u_\alpha) + \left(1 - \frac{1}{2\tau_k}\right) \partial_\beta \Pi_{\alpha\beta}^{k,(1)} = 0, \quad (\text{A13})$$

where $\Pi_{\alpha\beta}^{k,(1)} = \sum_i f_i^{k,(1)} e_{i\alpha} e_{i\beta}$ is the first-order momentum flux tensor and can be calculated by

$$\begin{aligned} \Pi_{\alpha\beta}^{k,(1)} &= \sum_i f_i^{k,(1)} e_{i\alpha} e_{i\beta} = -\tau_k \sum_i e_{i\alpha} e_{i\beta} D_{t_0} f_i^{k,\text{eq}} \\ &= -\tau_k \left\{ \partial_{t_0} (\rho_k u_\alpha u_\beta + p_k \delta_{\alpha\beta}) \right. \\ &\quad \left. + \partial_\gamma \left[\frac{1}{3} \rho_k c^2 (u_\alpha \delta_{\beta\gamma} + u_\beta \delta_{\alpha\gamma} + u_\gamma \delta_{\alpha\beta}) \right] \right\} \\ &= -\tau_k \left[-\partial_\gamma (\rho_k u_\alpha u_\beta u_\gamma) + \frac{1}{3} \rho_k c^2 (\partial_\alpha u_\beta + \partial_\beta u_\alpha) \right] \\ &\quad - \tau_k \left[\frac{1}{3} c^2 - (c_s^k)^2 \right] [u_\alpha \partial_\beta \rho_k + u_\beta \partial_\alpha \rho_k \\ &\quad + \partial_\gamma (\rho_k u_\gamma \delta_{\alpha\beta})], \\ &= -\frac{1}{3} \tau_k \rho_k c^2 (\partial_\alpha u_\beta + \partial_\beta u_\alpha) + O(\text{Ma}^3), \end{aligned} \quad (\text{A14})$$

where Ma is the Mach number, given by $\text{Ma} = u/c_s$. In the above result, the terms of $O(\text{Ma}^3)$ should be neglected in order to be consistent with the small-velocity expansion of $f_i^{k,\text{eq}}$ up to $O(\text{Ma}^2)$. Hence, Eq. (A13) becomes

$$\partial_{t_1} (\rho_k u_\alpha) + \partial_\beta \left[\frac{c^2}{3} \left(\tau_k - \frac{1}{2} \right) (\partial_\alpha u_\beta + \partial_\beta u_\alpha) \right] = 0. \quad (\text{A15})$$

Combining the zeroth- and first-order results together with $\partial_t = \partial_{t_0} + \epsilon \partial_{t_1}$, we can obtain the macroscopic governing equations as

$$\partial_t \rho_k + \partial_\alpha (\rho_k u_\alpha) = 0, \quad (\text{A16})$$

$$\begin{aligned} \partial_t (\rho_k u_\alpha) + \partial_\beta (\rho_k u_\alpha u_\beta + p_k \delta_{\alpha\beta}) \\ = \partial_\beta \left[\frac{c^2}{3} \left(\tau_k - \frac{1}{2} \right) \delta_t (\partial_\alpha u_\beta + \partial_\beta u_\alpha) \right], \end{aligned} \quad (\text{A17})$$

which are the exact continuity and momentum equations for single-phase flows if the kinematic viscosity ν_k is expressed as Eq. (12) in each single-phase region.

[1] S. O. Unverdi and G. Tryggvason, *J. Comput. Phys.* **100**, 25 (1992).
 [2] D. Juric and G. Tryggvason, *J. Comput. Phys.* **123**, 127 (1996).
 [3] G. Tryggvason, B. Bunner, A. Esmaeeli, D. Juric, N. Al-Rawahi, W. Tauber, J. Han, S. Nas, and Y.-J. Jan, *J. Comput. Phys.* **169**, 708 (2001).
 [4] C. Hirt and B. Nichols, *J. Comput. Phys.* **39**, 201 (1981).
 [5] W. J. Rider and D. B. Kothe, *J. Comput. Phys.* **141**, 112 (1998).

[6] D. Gueyffier, J. Li, A. Nadim, R. Scardovelli, and S. Zaleski, *J. Comput. Phys.* **152**, 423 (1999).
 [7] J. E. Pilliod Jr. and E. G. Puckett, *J. Comput. Phys.* **199**, 465 (2004).
 [8] S. Osher and J. A. Sethian, *J. Comput. Phys.* **79**, 12 (1988).
 [9] M. Sussman, E. Fatemi, P. Smereka, and S. Osher, *Comput. Fluids* **27**, 663 (1998).
 [10] S. Osher and R. P. Fedkiw, *Level Sets Methods and Dynamic Implicit Surfaces* (Springer, Berlin, 2003).

- [11] X. Yang, A. J. James, J. Lowengrub, X. Zheng, and V. Cristini, *J. Comput. Phys.* **217**, 364 (2006).
- [12] R. Scardovelli and S. Zaleski, *Annu. Rev. Fluid Mech.* **31**, 567 (1999).
- [13] X. He, S. Chen, and R. Zhang, *J. Comput. Phys.* **152**, 642 (1999).
- [14] H.-Y. Chen, D. Jasnow, and J. Viñals, *Phys. Rev. Lett.* **85**, 1686 (2000).
- [15] C. K. Aidun and J. R. Clausen, *Annu. Rev. Fluid Mech.* **42**, 439 (2010).
- [16] J. Zhang, *Microfluid. Nanofluid.* **10**, 1 (2011).
- [17] X. He and L.-S. Luo, *Phys. Rev. E* **55**, R6333 (1997).
- [18] S. Chen and G. D. Doolen, *Annu. Rev. Fluid Mech.* **30**, 329 (1998).
- [19] M. M. Dupin, I. Halliday, and C. M. Care, *Phys. Rev. E* **73**, 055701 (2006).
- [20] H. Kusumaatmaja, J. Léopoldès, A. Dupuis, and J. M. Yeomans, *Europhys. Lett.* **73**, 740 (2006).
- [21] H. Liu and Y. Zhang, *J. Comput. Phys.* **229**, 9166 (2010).
- [22] H. Liu and Y. Zhang, *Phys. Fluids* **23**, 082101 (2011).
- [23] W. Wang, Z. Liu, Y. Jin, and Y. Cheng, *Chem. Eng. J.* **173**, 828 (2011).
- [24] A. K. Gunstensen, D. H. Rothman, S. Zaleski, and G. Zanetti, *Phys. Rev. A* **43**, 4320 (1991).
- [25] D. H. Rothman and J. M. Keller, *J. Stat. Phys.* **52**, 1119 (1988).
- [26] D. Grunau, S. Chen, and K. Eggert, *Phys. Fluids A* **5**, 2557 (1993).
- [27] X. Shan and H. Chen, *Phys. Rev. E* **47**, 1815 (1993).
- [28] P. Yuan and L. Schaefer, *Phys. Fluids* **18**, 042101 (2006).
- [29] M. Sbragaglia, R. Benzi, L. Biferale, S. Succi, K. Sugiyama, and F. Toschi, *Phys. Rev. E* **75**, 026702 (2007).
- [30] A. Kupershtokh, D. Medvedev, and D. Karpov, *Comput. Math. Appl.* **58**, 965 (2009).
- [31] M. R. Swift, E. Orlandini, W. R. Osborn, and J. M. Yeomans, *Phys. Rev. E* **54**, 5041 (1996).
- [32] R. van der Sman and S. van der Graaf, *Comput. Phys. Commun.* **178**, 492 (2008).
- [33] R. Nourgaliev, T. Dinh, T. Theofanous, and D. Joseph, *Int. J. Multiphase Flow* **29**, 117 (2003).
- [34] H. Zheng, C. Shu, and Y. Chew, *J. Comput. Phys.* **218**, 353 (2006).
- [35] T. Inamuro, T. Ogata, S. Tajima, and N. Konishi, *J. Comput. Phys.* **198**, 628 (2004).
- [36] A. Fakhari and M. H. Rahimian, *Phys. Rev. E* **81**, 036707 (2010).
- [37] T. Lee and L. Liu, *J. Comput. Phys.* **229**, 8045 (2010).
- [38] H. Huang, H. Zheng, X.-Y. Lu, and C. Shu, *Int. J. Numer. Methods Fluids* **63**, 1193 (2010).
- [39] S. V. Lishchuk, C. M. Care, and I. Halliday, *Phys. Rev. E* **67**, 036701 (2003).
- [40] J. U. Brackbill, D. B. Kothe, and C. Zemach, *J. Comput. Phys.* **100**, 335 (1992).
- [41] M. Latva-Kokko and D. H. Rothman, *Phys. Rev. E* **71**, 056702 (2005).
- [42] L. Wu, M. Tsutahara, L. S. Kim, and M. Ha, *Int. J. Multiphase Flow* **34**, 852 (2008).
- [43] T. Reis and T. N. Phillips, *J. Phys. A* **40**, 4033 (2007).
- [44] J. Tölke, M. Krafczyk, M. Schulz, and E. Rank, *Philos. Trans. R. Soc. London* **360**, 535 (2002).
- [45] I. Halliday, R. Law, C. M. Care, and A. Hollis, *Phys. Rev. E* **73**, 056708 (2006).
- [46] I. Halliday, A. P. Hollis, and C. M. Care, *Phys. Rev. E* **76**, 026708 (2007).
- [47] S. V. Lishchuk, I. Halliday, and C. M. Care, *Phys. Rev. E* **77**, 036702 (2008).
- [48] M. Latva-Kokko and D. H. Rothman, *Phys. Rev. E* **72**, 046701 (2005).
- [49] M. Mendoza, F. K. Wittel, and H. J. Herrmann, *Eur. Phys. J. E* **32**, 339 (2010).
- [50] C.-H. Shih, C.-L. Wu, L.-C. Chang, and C.-A. Lin, *Philos. Trans. R. Soc., A* **369**, 2510 (2011).
- [51] G. I. Taylor, *Proc. R. Soc. London, Ser. A* **138**, 41 (1932).
- [52] J. Li, Y. Y. Renardy, and M. Renardy, *Phys. Fluids* **12**, 269 (2000).
- [53] H. P. Grace, *Chem. Eng. Commun.* **14**, 225 (1982).
- [54] P. V. Puyvelde, H. Yang, J. Mewis, and P. Moldenaers, *J. Rheol.* **44**, 1401 (2000).
- [55] V. Cristini, S. Guido, A. Alfani, J. Blawdziewicz, and M. Loewenberg, *J. Rheol.* **47**, 1283 (2003).
- [56] A. Vananroye, R. Cardinaels, P. V. Puyvelde, and P. Moldenaers, *J. Rheol.* **52**, 1459 (2008).
- [57] J. M. Rallison, *J. Fluid Mech.* **109**, 465 (1981).
- [58] A. Vananroye, P. Van Puyvelde, and P. Moldenaers, *Langmuir* **22**, 3972 (2006).
- [59] P. J. A. Janssen and P. D. Anderson, *Phys. Fluids* **19**, 043602 (2007).
- [60] P. J. A. Janssen, A. Vananroye, P. V. Puyvelde, P. Moldenaers, and P. D. Anderson, *J. Rheol.* **54**, 1047 (2010).
- [61] R. Clift, J. R. Grace, and M. E. Weber, *Bubbles, Drops, and Particles* (Academic Press, New York, 1978).
- [62] D. Bhaga and M. E. Weber, *J. Fluid Mech.* **105**, 61 (1981).
- [63] Z. Guo, C. Zheng, and B. Shi, *Phys. Rev. E* **65**, 046308 (2002).
- [64] S. Succi, *The Lattice Boltzmann Equation For Fluid Dynamics and Beyond* (Oxford University Press, Oxford, 2001).
- [65] L. Amaya-Bower and T. Lee, *Comput. Fluids* **39**, 1191 (2010).
- [66] J. Hua, J. F. Stene, and P. Lin, *J. Comput. Phys.* **227**, 3358 (2008).
- [67] D. D. Joseph, *J. Fluid Mech.* **488**, 213 (2003).
- [68] R. M. Davies and G. Taylor, *Proc. R. Soc. London, Ser. A* **200**, 375 (1950).
- [69] D. Rodrigue, *AIChE J.* **47**, 39 (2001).